Chemosphere 290 (2022) 133296

Contents lists available at ScienceDirect

Chemosphere

journal homepage: www.elsevier.com/locate/chemosphere

Synthesis and catalytic properties of calcium oxide obtained from organic ash over a titanium nanocatalyst for biodiesel production from dairy scum

Walid Nabgan[a,b,*], Bahador Nabgan[a,b], Muhammad Ikram[c,**], Arvind H. Jadhav[d,***], Mohamad Wijayanuddin Ali[a,b,****], Anwar Ul-Hamid[e], Hyungseok Nam[f], Parashuram Lakshminarayana[g], Ankit kumar[h], Mahadi B. Bahari[i], Nur Farahain Khusnun[a,b]

[a] *School of Chemical and Energy Engineering, Faculty of Engineering, Universiti Teknologi Malaysia, 81310, Skudai, Johor, Malaysia*
[b] *Centre of Hydrogen Energy, Institute of Future Energy, Universiti Teknologi Malaysia, 81310, Skudai, Johor, Malaysia*
[c] *Solar Cell Applications Research Lab, Department of Physics, Government College University Lahore, 54000, Punjab, Pakistan*
[d] *Centre for Nano and Material Science, JAIN University, Jain Global Campus, Bangalore, 562112, Karnataka, India*
[e] *Core Research Facilities, King Fahd University of Petroleum & Minerals, Dhahran, 31261, Saudi Arabia*
[f] *Greenhouse Gas Laboratory, Korea Institute of Energy Research, Dajeon, 34129, Republic of Korea*
[g] *Department of Chemistry, New Horizon College of Engineering Affiliated to VTU, Bangalore, 560087, India*
[h] *Department of Chemical Engineering and Technology, Indian Institute of Technology (BHU), Varanasi, UP, 221005, India*
[i] *Faculty of Science, Universiti Teknologi Malaysia, 81310, UTM Johor Bahru, Johor, Malaysia*

HIGHLIGHTS

- Biodiesel production from dairy scum over Ca–Ti catalysts has been studied.
- The 3Ca–3Ti nano-catalyst exhibited bifunctional acid-base properties.
- A biodiesel yield of 97.2% is achieved for the 3Ca–3Ti nano-catalyst.
- The physical properties of the produced biodiesel are within the EN14214 standards.

GRAPHICAL ABSTRACT

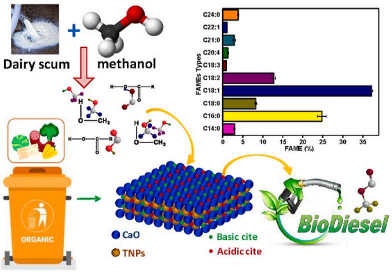

ARTICLE INFO

Handling Editor: Derek Muir

Keywords:
Biodiesel
Organic ash
Acid-base catalysts

ABSTRACT

The fatty acid methyl ester (FAME) production from dairy effluent scum as a sustainable energy source using CaO obtained from organic ash over titanium dioxide nanoparticles (TNPs) as the transesterification nano-catalyst has been studied. The physical and chemical properties of the synthesized catalysts were characterized, and the effect of different experimental factors on the biodiesel yield was studied. It was revealed that the CaO–TiO_2 nano-catalyst displayed bifunctional properties, has both basic and acid phases, and leads to various effects on the catalyst activity in the transesterification process. These bifunctional properties are critical for achieving simultaneous transesterification of dairy scum oil feedstock. According to the reaction results, the catalyst

---

[*] Corresponding author. School of Chemical and Energy Engineering, Faculty of Engineering, Universiti Teknologi Malaysia, 81310, Skudai, Johor, Malaysia.
[**] Corresponding author.
[***] Corresponding author.
[****] Corresponding author. School of Chemical and Energy Engineering, Faculty of Engineering, Universiti Teknologi Malaysia, 81310, Skudai, Johor, Malaysia.
E-mail addresses: wnabgan@gmail.com (W. Nabgan), dr.muhammadikram@gcu.edu.pk (M. Ikram), j.arvind@jainuniversity.ac.in (A.H. Jadhav), mwali@utm.my (M.W. Ali).

https://doi.org/10.1016/j.chemosphere.2021.133296
Received 21 June 2021; Received in revised form 8 December 2021; Accepted 11 December 2021

Transesterification
Dairy scum

without and with a low ratio of TNPs showed a low catalytic activity. In contrast, the 3Ca–3Ti nano-catalyst had the highest catalytic activity and a strong potential for reusability, producing a maximum biodiesel yield of 97.2% for a 3 wt% catalyst, 1:20 oil to methanol molar ratio for the dairy scum, and a reaction temperature of 70 °C for a period of 120 min under a 300 kPa pressure. The physical properties of the produced biodiesel are within the EN14214 standards.

Abbreviation

Al_2O_3	Aluminium oxide
ASTM	American society for testing and materials
BET	Brunauer, Emmett and Teller
C14	0: Myristic acid
C16	0: Palmitoleic acid
C18	0: Stearic acid
C18	1: Oleic acid
C18	1: Oleic acid
C18	2: Linoleic acid
C18	3: Linolenic acid
C20	4 ω6: Arachidonic acid
C21	0: Heneicosanoic acid
C22	1: Erucic acid
C24	0: Lignoceric acid
$Ca_3(Ti_2O_7)$	Tricalcium dititanate
$CaCO_3$	Calcium carbonate
CaO	Calcium oxide
CHNS	Carbon, hydrogen, nitrogen, sulphur, and oxygen analyzer
CI	Confidence interval
CO_2-TPD	Temperature-programmed desorption of carbon dioxide
E_a	Activation energy
EA	Elemental analyzer
EN	European Norm
FAME	Fatty acid methyl ester production
FTIR	Fourier transform infrared
GC/MS	Gas chromatography-mass spectrometry
H_2-TPR	Temperature programmed reduction of hydrogen
He	Helium
HRTEM	High-resolution transmission electron microscopy
ICDD	International center for diffraction data
JCPDS	Joint committee on powder diffraction standards
K_2CO_3	Potassium carbonate
KBr	Potassium bromide
kpa	Kilopascal
M	Molar concentration
MgO	Magnesium oxide
NaOH	Sodium hydroxide
NH_3-TPD	Temperature-programmed desorption of ammonia
NiO	Nickel(II) oxide
NOx	Nitrogen oxides
rpm	Revolutions per minute
SEM	Scanning electron microscope
SrO	Strontium oxide
TEM	Transmission electron microscopy
TGA	Thermogravimetric analysis
TiO_2	Titanium dioxide
TNPs	Titanium dioxide nanoparticles
WL:	Weight loss
WOS	Web of science
wt. %	Weight percent
XPS	X-ray photoelectron spectroscopy
XRD	X-Ray Diffraction
XRF	X-ray fluorescence
ZnO	Zinc oxide

1. Introduction

Fossil fuel resources are non-renewable and limited, and their applications trigger environmental issues like acid rain, global warming, and greenhouse gas pollution (Dawood et al., 2021; Helmi et al., 2021). Therefore, research into sustainable alternatives (such as biofuels) to fossil fuels has become essential in recent decades. Biodiesel seems to have the ideal physicochemical features and is comparable to traditional petrodiesel (Mofijur et al., 2021; Yusuff et al., 2021). Researchers have established and evaluated various biodiesel feedstocks to meet the energy need, including fish oil, brown grease, yellow grease, chicken fat, pork lard, poultry fat, and beef tallow. Biodiesel made from animal fats is a possible alternative fuel for compressed ignition engines (Srikanth et al., 2020). A dairy processing around half a million liters of milk every 24 h will generate around 200–350 kg of dairy waste a day, making it extremely difficult to convert and use this plentiful dairy waste. Biodiesel from this dairy scum will lower generation costs and solve the dumping issues of dairies (Channappagoudra, 2021).

Transesterification necessitates the use of a catalyst to speed up the chemical reaction (Son and Yeom, 2021). Both acid and base catalysts may be categorized as homogeneous, heterogeneous, or enzymatic catalysts based on their physicochemical properties (Amini et al., 2017; Thangarasu and Anand, 2019; Ong et al., 2021). Appropriately assisted catalysts should be designed to increase catalyst efficiency, avoid unnecessary leaching of active species, and block the catalyst with reaction by-products (Marinković et al., 2017). Heterogeneous catalysts have many advantages, such as the capability to be reused, which could result in a higher biodiesel yield (Abdullah et al., 2022). Supported catalysts made from organic waste, such as vegetable waste and fruit peel, are ideal for biodiesel production (mesoporosity, uniform pore scale, well-defined pore shape) and are of particular interest, as such wastes are being produced in the high amount of a million metric tons every year in the world (Sagar et al., 2018). Fly ash-supported CaO catalysts were recently tested for biodiesel synthesis from various plant oils and found to be powerful and reliable (Ho et al., 2014; Hadiyanto et al., 2016), and they have received significant attention due to their low cost and high activity. However, the drawback of CaO is that its performance is affected by calcium ions in the polar phase, which suffers from leaching (Kouzu et al., 2009). To solve this issue, CaO can be loaded on the proper support to resolve this limitation and increase stability (Dehghani et al., 2019; Pavlović et al., 2020). Titanium dioxide nanoparticles (TNPs) may be used in the transesterification reaction because of their wide surface size, acid-base properties, good metal-support interactions, non-toxicity, low production cost, and chemical stability (Carlucci et al., 2019; Khaligh et al., 2021). As stated in Table 1, to the best of our knowledge and according to the literature survey, very few works have been published on converting dairy waste to biodiesel over organic ash-assisted TiO_2 heterogeneous catalysts. Hence, these two parameters, namely low-cost catalysts and dairy scum oil recycling, play a vital role in the economic and environmental impact of the biodiesel generation technology. This study examined the influence of CaO (obtained from organic ash) to TNP nano-catalyst ratios on the chemical

Table 1
Summary of some published papers (1970–2021) in the WOS database by employing the title search to keywords such as “biodiesel”, “dairy”, and “scum”.

No.	Year	Main focus	Ref.
1	2017	“Bio-based diluents improve cold flow properties of dairy washed milk-scum biodiesel” ● The influence of ethyl levulinate and acetoacetate was tested on the low-temperature properties of dairy washed milk scum biodiesel. ● The flash point, induction period, acid value, and viscosity of the produced biodiesel were within the acceptable limits of the biodiesel standard (ASTM D6751-15c).	Srikanth et al. (2017)
2	2018	“Sodium phosphate synthesis through glycerol purification and its utilization for biodiesel production from dairy scum oil to economize production cost” ● The maximum dairy scum oil methyl ester yield of 97.7% was achieved. ● The activation energy (E_a) of the transesterification reaction was found to be 35.56 kJ mol^{-1}.	Yatish et al. (2018)
3	2019	“The effects of graphene oxide nanoparticle additive stably dispersed in dairy scum oil biodiesel-diesel fuel blend on CI engine: performance, emission and combustion characteristics” ● Sodium dodecyl sulfate was used as a surfactant for a steady dispersion of graphene oxide nanoparticles in the fuel blends. ● The addition of graphene nanoparticles in dairy scum oil methyl ester fuel blends resulted in a significant reduction in the combustion duration, ignition delay period, improvement in the peak pressure, and heat release rate at the maximum load condition.	Soudagar et al. (2019)
4	2019	“High lipid accumulating bacteria isolated from dairy effluent scum grown on dairy wastewater as potential biodiesel feedstock” ● The effect of different carbon sources on the lipid accumulation capacity of the bacterial isolates was evaluated. ● The lipids accumulated by bacteria were mostly neutral lipids and contained fatty acids of chain length C14:0-C18:0. ● The transesterified bacterial lipids from the isolated bacteria are suitable for biodiesel applications.	Behera et al. (2019)
5	2020	“Optimization and kinetic study of biodiesel production from Hydnocarpus wightiana oil and dairy waste scum using snail shell CaO nano catalyst” ● Response surface methodology is used to optimize the reaction parameter that affects the transesterification process for the biodiesel yield. ● A comprehensive kinetic study for the transesterification reaction was performed at different temperatures (50–65 °C) for the methanolysis of scum oil and Hydnocarpus wightiana oil catalyzed by CaO nanoparticles. ● The recovered CaO nanocatalyst is reused five times with substantial loss in the biodiesel yield.	Krishnamurthy et al. (2020)
6	2021	● The FAME production from dairy scum using CaO obtained from organic ash over TNPs as the transesterification nano-catalyst has been studied. ● The physical and chemical properties of the catalysts were characterized by XRD, BET, TEM, FTIR, CO_2-TPD, H_2-TPR, NH_3-TPD, CHNS, and TGA. ● The CaO–TiO_2 nano-catalyst displayed bifunctional properties, having both basic and acid phases. ● The main properties of the biodiesel products were determined and were consistent with EN 14214 standards.	Current study

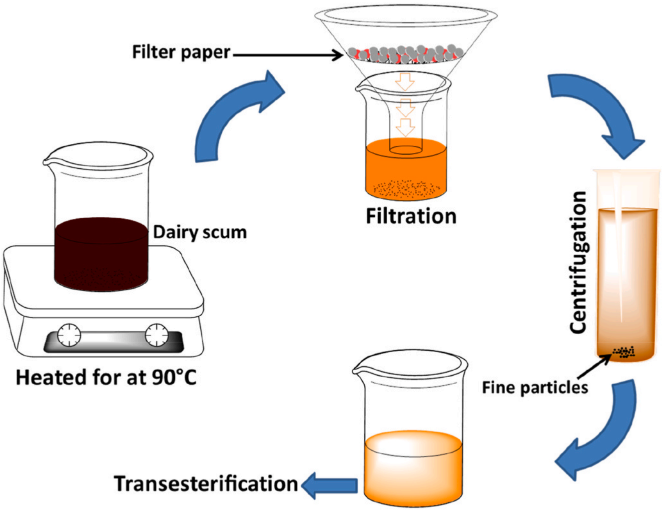

Fig. 1. Dairy scum pre-treatment.

Fig. 2. Preparation of CaO/TiO_2 nanocatalysts.

and physical properties of the catalysts and their biodiesel generation from dairy waste scum. Synthesized fresh catalysts were characterized by XRD, BET, TEM, CO_2-TPD, H_2-TPR, FTIR, and NH_3-TPD, and the spent catalysts were analyzed by CHNS and TGA. The influence of reaction parameters like temperature, catalyst loading, reusability, pressure, and methanol amount on the yield of FAME was evaluated. The physicochemical characteristics of the produced biodiesel were also investigated. As a result, using CaO as a heterogeneous catalyst derived from organic waste over TNPs to convert dairy waste scum to biodiesel will increase sustainability by generating a value-added product.

2. Experimental

2.1. Pre-treatment of dairy scum

The dairy waste was collected from the Pak dairy company, Tehran, Iran. As shown in Fig. 1, it was heated for 1 h at 90 °C and then cooled before moving it to a separating funnel. The solid particles in the bottom aqueous layer were removed. The top oil layer was separated via a centrifugal force at 7000 rpm for 20 min to remove the fine elements. The clear dairy scum oil was utilized for the transesterification reaction.

2.2. Synthesis of calcium oxide and titanium nanocatalysts

CaO was synthesized by burning fruit peel and vegetable waste at 1000 °C for 3 h after washing them from the dirt. The preparation steps are shown in Fig. 2. According to our previous research (Nabgan et al., 2021), nanostructured CaO and TiO_2 catalysts were synthesized via a hydrothermal treatment. Briefly, 5 M NaOH was dissolved and mixed for 1 h in 100 mL of deionized water, and then a specific quantity of CaO and TiO_2 was mixed with 100 mL of deionized water for dilution purposes with a 1:10 mass ratio and stirred for a couple of hours individually in two different beakers. Both liquid solutions were then gently poured into two Teflon cylinders, sealed in autoclave reactors, and heated at 140 °C for 48 h. Those autoclave reactors were then cooled down to room temperature, and the prepared liquid samples were filtered and washed with deionized water until the washing water's pH reached 6. Then, they were dried for 24 h at 110 °C. Both samples were then calcined at 800 °C for 3 h. According to our published works, the prepared nanostructured CaO and TiO_2 were then impregnated (Nabgan et al., 2017a, 2017b, 2020). In brief, four catalysts were synthesized with the CaO to TiO_2 mass ratios of 3:0, 3:1, 3:2, and 3:3 and named Ca, 3Ca–1Ti, 3Ca–2Ti, and 3Ca–3Ti, respectively. Next, the nano CaO and TiO_2 samples were gently poured into 150 mL of deionized water while stirring at 95 °C until the water evaporated and the solution changed to a slurry. The muddy samples were then dried overnight at 110 °C and calcined at 800 °C for 4 h.

2.3. Catalyst characterization

The crystalline structure of the samples was characterized by X-ray powder diffraction (XRD) measurements using a Bruker D8 Advance diffractometer (Cu Kα radiation, $\lambda = 1.5406$ Å). The diffraction data were collected in a 2 theta range of 5° to 90°. The obtained patterns were distinguished with the reference patterns in the JCPDS-ICDD (International Center for Diffraction Database) by the X'Pert Highscore Plus software to perform the phase identification, and the crystal size was calculated via the Scherrer equation. N_2 physisorption isotherms were used to analyze the specific surface area (BET method), pore-volume, and pore size distributions on the Micromeritics TriStar II equipment. The catalysts were previously subjected to a vacuum degassing treatment at 250 °C for 12 h. The reducibility, acidity, and basicity of the catalysts were investigated using the Micromeritics Chemisorb 2720 apparatus. The specifics of these three characterizations were previously published by our co-authors (Nabgan et al., 2016a, 2016b). Fourier transform infrared (FTIR) absorption spectra from 400 to 4000 cm^{-1} were obtained on a Shimadzu IR-Prestige-21 spectrometer utilizing pure KBr as a reference background to record the surface functional groups after the preparation of the catalyst. HRTEM micrographs were obtained with a JEOL JEM-ARM200F instrument at 200 kV. The carbon content of the spent catalysts was determined via CHNS elemental analysis, and the surface area was determined by using a Flowsorb III surface area analyzer. The mass loss of the spent catalysts was analyzed by the Shimadzu TG-50 thermogravimetric equipment, which points out the carbon formation during the transesterification. 10 mg of the catalysts was placed in a crucible and heated to 800 °C at a heating rate of 20 °C min^{-1} under ambient conditions using airflow.

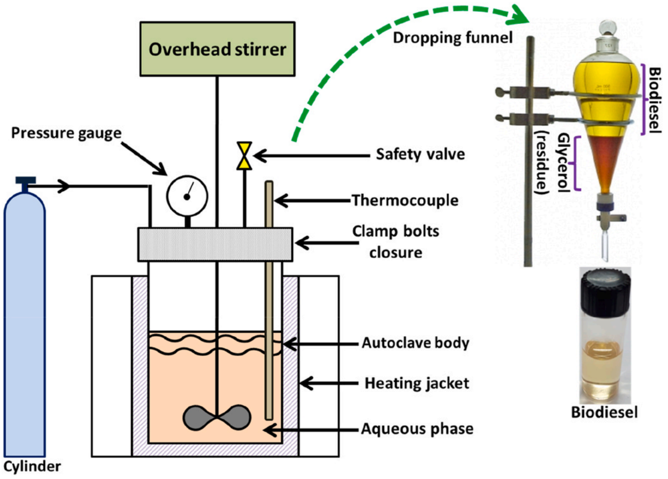

Fig. 3. Schematic diagram of the system employed for the transesterification of dairy scum (Parr benchtop reactor 4560).

2.4. Catalytic transesterification of dairy scum

Oil derived from dairy scum and a specific amount of methanol was loaded into a Parr benchtop reactor model 4560 reactor equipped with an autoclave and an overhead stirrer. The schematic image of the transesterification process is presented in Fig. 3. First, the reactor was capped tightly to avoid leaking of the methanol; then, it was heated in a surrounded heating jacket, and a thermometer monitored the reaction temperature. The reaction took place in the presence of a 1 to 5 wt% heterogeneous catalyst under continuous stirring at different temperatures (50 °C–90 °C) with oil to methanol molar ratios of 1:5 to 1:30, a reaction time of 60–300 min, and a pressure of 100–500 kPa. The reactor's pressure was measured by a pressure gauge using a cylinder of nitrogen gas. To keep the process homogeneous, the reaction mixture was whisked at 600 rpm. The machine was automatically cooled to room temperature after the procedure was finished. The liquid sample in the reactor was then poured into the separation funnel and permitted to settle until two layers were created: the upper phase was biodiesel, while the bottom phase included glycerol, unreacted methanol, and other byproducts. Finally, the biodiesel was removed and analyzed, and the used catalysts were collected from the lower phase by a filtration procedure. The percentage yield of biodiesel was obtained by using the equation below:

$$Biodiesel\ Yield\ (\%) = \frac{Biodiesel\ amount}{Scum\ oil\ weight} \times 100$$

2.5. Product analysis

Qualitative analysis and validation readings were acquired from a GC/MS Agilent 7890B. The Rtx-5MS capillary column (29.5 m length, 0.25 μm thickness, and 0.25 mm diameter) was used to analyze the FAME content in the biodiesel. Helium (He) gas with a flow rate of 1.5 mL min^{-1} was used and combined with a programmed column temperature range of 120–300 °C at 10 °C min^{-1}. FAME was calculated by associating the peak areas between the samples with those of the standard compounds. All tests were repeated three times, and the average was selected, with a standard error of less than 5% in determining the biodiesel yield. The chemical and physical properties of the biofuel produced were assessed under the specifications of the European standard EN-14214 (Barabás and Todoruţ, 2011) by utilizing atomic absorption spectrometry, infrared spectroscopy, and gas chromatography-mass spectrometry analyses. Properties of the biodiesel were characterized accordingly, i.e., density (kg m^{-3}) with the density meter, kinematic viscosity ($mm^2\ s^{-1}$) with the ASTM D445

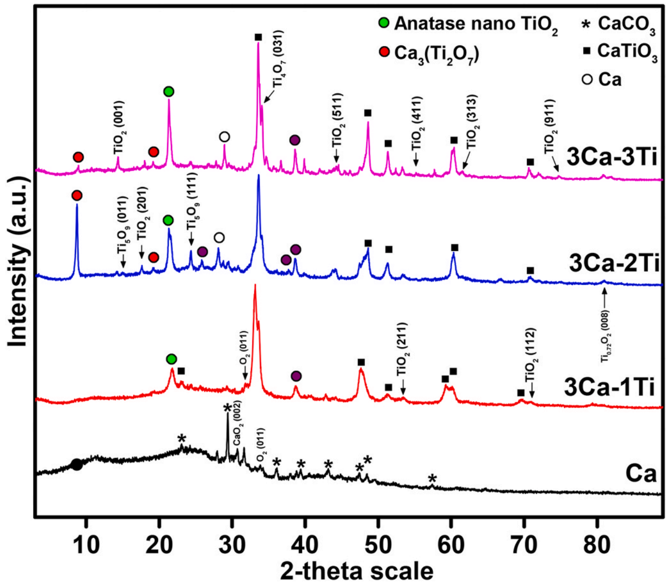

Fig. 4. XRD pattern for the CaO–TiO_2 nanocatalysts.

method, flash point (°C) with the ASTM D93 method, cloud point (°C) with the ASTM D2500, cetane number with the ASTM D6890 method, sulphur content (wt.%) with Multi EA 5000, and ash content (wt.%) with the ASTM D874 method,.

3. Result and discussions

3.1. *Fresh nanocatalyst characterization*

The X-ray diffraction (XRD) curves were obtained to study the crystalline properties of Ca–Ti nanomaterials. The obtained patterns are shown in Fig. 4, and the average crystal size is shown in Table 2. The XRD curve of the Ca sample shows characteristics peaks at 2θ angles of 23.12°, 29.4°, 36.1°, 39.42°, 43.14°, 47.44°, 48.48°, and 57.38° corresponding to (012), (104), (110), (113), (202), (018), (116), and (122) diffraction planes of the cubical phase, respectively, which are in good agreement with the standard ICDD card number 01-086-2334 for calcite ($CaCO_3$) (Deyab et al., 2018). $CaCO_3$ peaks were greatly reduced after TNPs were impregnated in the rest of the catalysts, indicating that calcium oxide nanoparticles are heavily scattered or have developed an amorphous phase on the mesoporous support surface, which is outside the detection limit of the XRD study. By introducing TNPs, crystalline peaks developed at 23.16°, 33.14°, 47.72°, 59.38°, 60.28°, and 69.66° corresponding to (002), (112), (220), (132), (312), and (224) diffraction planes of the cubic calcium titanium oxide ($CaTiO_3$) structure, respectively, which matched with the ICDD card number 01-081-8565. The TiO_2 (ICDD card number: 01-070-2556) phases were detected at a 2θ angle of 38.7° (Durdu, 2019), and the tetragonal phase of anatase nano TiO_2 was detected at a 2θ angle of 21.34° corresponding to the (101) plane with the ICDD card number 00-064-0863. The tricalcium dititanate ($Ca_3(Ti_2O_7)$) phase was also seen at 2θ angles of 8.74° and 19.02° (ICDD card number: 01-089-1384), which is unstable concerning calcium oxide (Mines, 1955). Ca, which matched with the ICDD card

Table 2

BET surface area, pore volume, average pore diameter, basicity, reducibility, acidity, and crystal size data of nanocatalysts.

Catalyst	Crystal size (nm)	Surface area (m^2. g^{-1})	Pore-volume (cm^3. g^{-1})	Pore-diameter (nm)	CO_2 uptake (mmol. g^{-1})	H_2-Consumption (mmol. g^{-1})	NH_3 uptake (mmol. g^{-1})
Ca	36.60	5.99	0.03	20.60	1.01	988.10	7.13
3Ca–1Ti	29.60	22.76	0.13	23.30	0.06	12.90	0
3Ca–2Ti	33.90	15.21	0.06	16.70	0.34	172	0
3Ca–3Ti	42.50	7.93	0.03	13.90	2.64	900.20	7.28

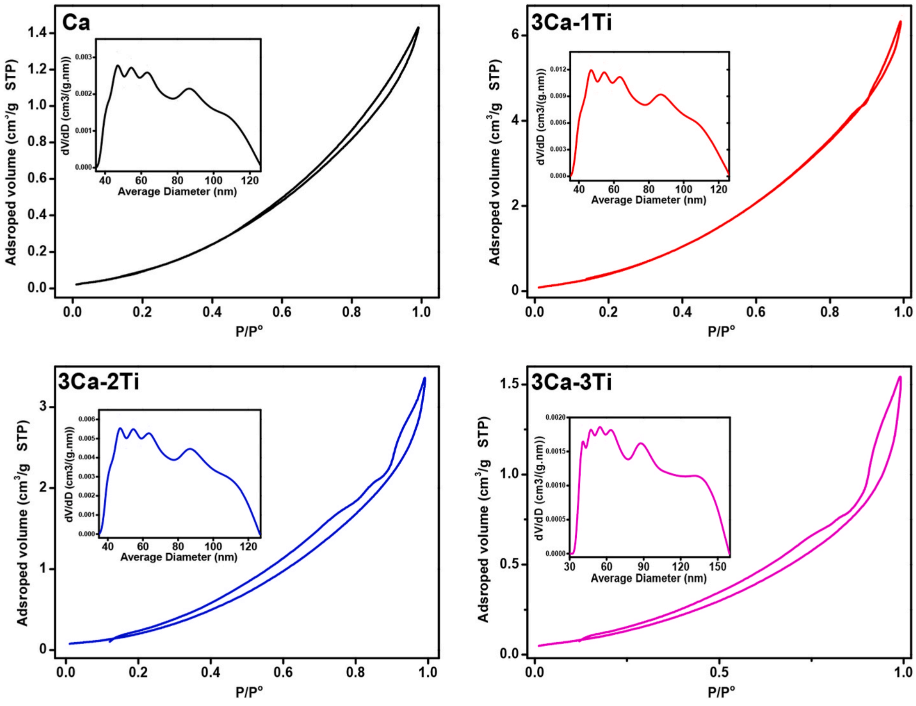

Fig. 5. Nitrogen adsorption isotherm and pore size distribution of the CaO–TiO_2 nanocatalysts.

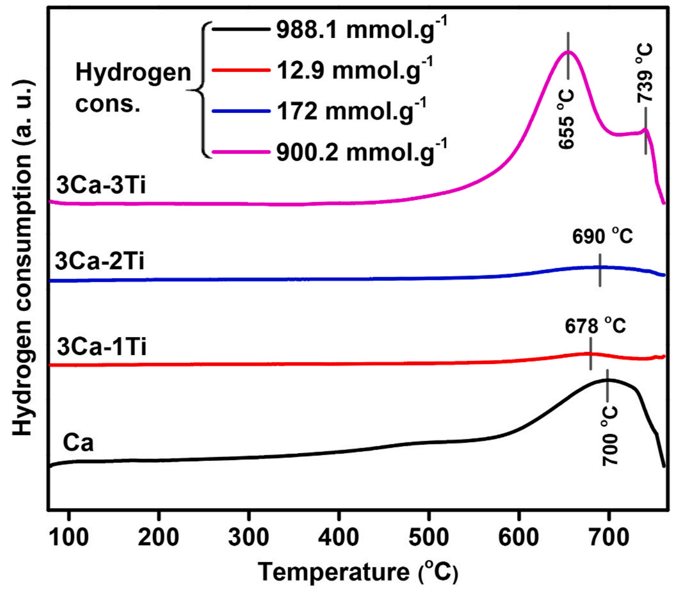

Fig. 6. Temperature-programmed reduction (H_2-TPR) curves of the CaO–TiO_2 nanocatalysts.

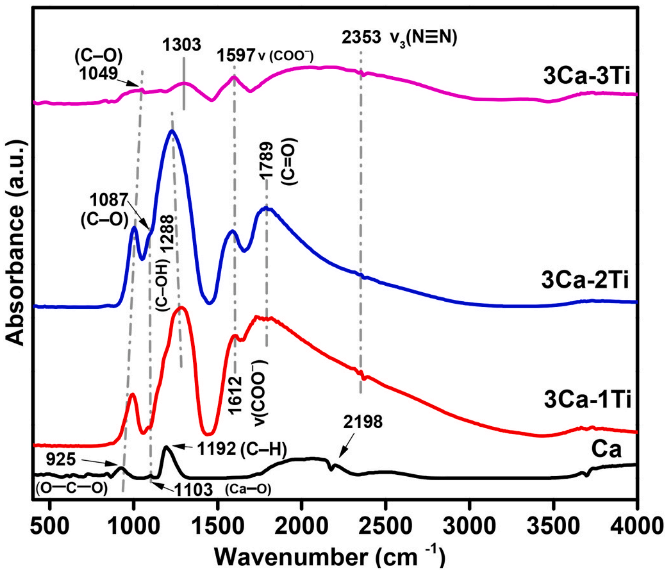

Fig. 7. FTIR curves of CaO–TiO_2 nanocatalysts.

number 01-077-7215 at a 2θ angle of 28.12°, was successfully formed and crystallized after calcination for the 3Ca–2Ti and 3Ca–3Ti samples. There were no traces of $CaCO_3$, proving that the organic ash produced pure Ca when impregnating with TNPs.

The structural properties of Ca–Ti nanocatalysts are presented in Table 1, and the adsorption-desorption isotherms and the pore size distribution patterns are shown in Fig. 5. As can be seen, the 3Ca–1Ti catalysts possessed the highest specific surface area (22.76 m^2 g^{-1}), pore-volume, and pore diameter. The results illustrated that the higher ratio of TNPs caused notable drops to the BET surface area. However, the total pore volume, indicating some TNPs with particle sizes smaller than the CaO pores, is loaded into the mesopores and microphones. This is not surprising because higher concentrations of TNPs result in the deposition of more Ti on the surface of CaO or the clogging of CaO pores by TNP species, thereby decreasing the surface area. TNPs interacting with CaO cause changes in the mesoporous structure, which may also be responsible for the decrease in the surface area and pore volume. The nitrogen adsorption/desorption curves reveal that Ca–Ti nanoparticles have an IV-type isotherm with an H4 hysteresis loop. These findings indicate that Ca–Ti nanocatalysts have both mesoporous configurations and solid contain particles. The form of the hysteresis loops shifted from H4 to H1 after increasing the TNP ratio. The creation of the new hysteresis loop could cause some structural faults in their mesoporous matrix. It is seen that the Ca, 3Ca–1Ti, and 3Ca–2Ti nanocatalysts have mesoporous structures with a multipeak pore size distribution between 40 and 100 nm and a maximum located at around 46 nm. The pore size distribution of the 3Ca–3Ti sample shifted to smaller values (30–90 nm). This result may be due to the large pores being partly occupied by the increasing Ti clusters. In conclusion, mesoporous Ca–Ti catalysts were successfully synthesized in this work.

The reducibility behavior of the CaO–TiO_2 catalysts was studied by the H_2-TPR technique and identified from their profiles (Fig. 6) and the related overall H_2 consumption (Table 1). As can be seen, the TPR curves for all respective samples show peaks above 500 °C, which are assigned to the CaO reduction with a strong interaction with TNPs. For the Ca sample, the peak observed at around 700 °C was associated with the decomposition process of $CaCO_3$, which is formed due to CaO carbonation (Bellido et al., 2009). It is worth noting that the CaO, which was previously undetectable in the XRD patterns, now exists and is reduced at higher temperatures. The results indicate that the addition of TNPs reduced the intensity for the 3Ca–1Ti and 3Ca–2Ti catalysts mainly because the TNP component inhibits the spinel phase formation for those two samples. Besides, the broad reduction shoulders for the 3Ca–1Ti (12.9 mmol g^{-1}) and 3Ca–2Ti (172 mmol g^{-1}) catalysts were shifted to lower temperatures at 678 °C and 690 °C, which means that the reducibility of CaO was promoted after the loading of TNPs. The 3Ca–3Ti TPR profile with the highest H_2 consumption (900.2 mmol g^{-1}) had two peaks at 655 °C and 739 °C, which may be attributed to the reduction of the TiO_2 rich 3Ca–3Ti mixture oxide related to the shoulder peak at 739 °C, and the prominent peak can be assigned to the reduction of CaO. This indicates that novel interactions influence the decline of the CaO–TiO_2 (3Ca–3Ti) catalysts. The TPR patterns demonstrated the variation of the CaO–TiO_2 interactions and the reducibility of different catalysts.

The FTIR spectra utilizing the KBr pellet method were conducted in the wavenumber range of 4000 to 500 cm^{-1} to inspect functional clusters present in the synthesized CaO–TiO_2 nanocatalysts, as shown in Fig. 7. The presence of the absorptions at 925 cm^{-1} for the Ca catalyst represented a characteristic absorption for the β-glycosidic bonds (Meng et al., 2019). The shift to a higher wavenumber at 1049 cm^{-1} by introducing TNPs to the catalysts (*C*–O absorption, alkoxy) originates from the $\rho r(CH_3)$ vibrations (Hasan et al., 2003). These two bands could be assigned to the stretching and bending vibrations of the calcium-oxygen bond, namely, the asymmetric vibrations of ν_s(CO–O–C) (1049 cm^{-1}) (Kochan et al., 2015) that is shifted from the symmetric stretching vibrations of O–*C*–O (925 cm^{-1}). The peaks at 1103 cm^{-1} in the spectra of bare CaO can be assigned to the Ca–O bond vibrations, which then shifted to a lower wavenumber for the 3Ca–1Ti and 3Ca–2Ti nanocatalysts at 1087 cm^{-1} due to the stretching vibration of C–O (Li and Cao, 2011). These are carbonates and are evident in the first three samples, which then disappeared for the 3Ca–3Ti nanocatalysts. The 1192 cm^{-1} bands are allocated to *C*–H angular deformations, which shifted to 1288 cm^{-1} (C–OH (Cao and Zhang, 2015)) for the 3Ca–1Ti and 3Ca–2Ti nanocatalysts because of the existence of monodentate nitrate ($\nu(NO_3)$) on the catalyst surface. However, these peaks also disappeared upon further increase of the TNP ratio and caused the formation of *C*–C stretching vibrations of acetylide (μ3-η2–CCH) for the 3Ca–3Ti nanocatalyst. The formation of acetylide is favorable, as it rationally accounts for the cleavage of C–O bonds during the reaction (Waheed et al., 2019). Except for the bare Ca, the appearance of the 1612 cm^{-1} band, which is correlated to aromatic rings (Ahmed et al., 2013) and the 1597 cm^{-1} band for the 3Ca–3Ti sample, are attributed to Lewis acid sites and can be assigned to the $\nu(COO^-)$ mode of acetate,

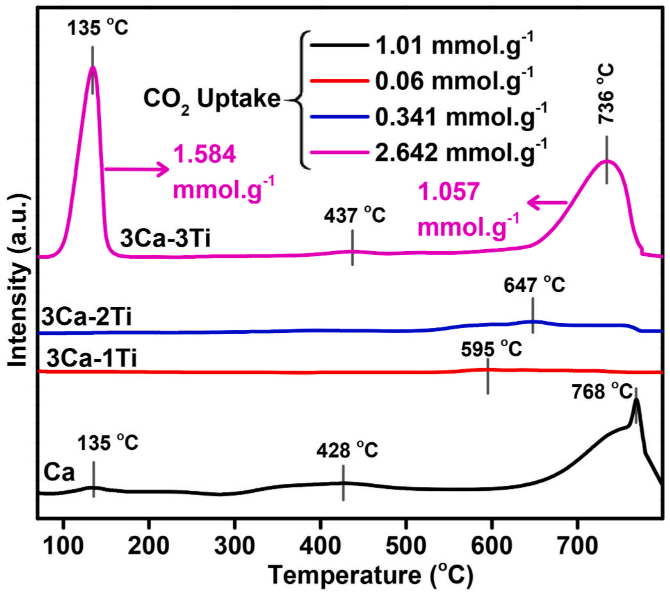

Fig. 8. Temperature-programmed desorption of CO_2 (CO_2-TPD) curves of the CaO–TiO_2 nanocatalysts.

indicating a significant interaction with the surface oxide. The stronger absorption close to 1789 cm^{-1} is linked to the unreacted isotopic nitric oxide molecule ($^{15}N^{18}O$) (Krim et al., 2000) or imide group C=O symmetric stretching (Zhang et al., 2017). Finally, the $\nu_3(N{\equiv}N)$ band at 2353 cm^{-1}, which has been ascribed to the N_2 species adsorbed on Lewis acid phases (Wakabayashi et al., 1997), indicates the possibility of the presence of illite (Daroughegi Mofrad et al., 2018).

Temperature-programmed desorption of CO_2 (CO_2-TPD) was implemented to characterize the basicity of the synthesized samples. The outcomes are presented in Fig. 8, and the quantitative CO_2 uptake is shown in Table 1. In the Ca curve, some CO_2 desorption is detected at very high temperatures, 768 °C with 1.01 mmol g^{-1} CO_2 uptake. This constituent contributes, alongside desorbed CO_2, to the broad TCD desorption peak located above 700 °C. This peak might be due to CO_2 formation by $CaCO_3$ decomposition to CaO rather than CO_2 adsorbed in the TPD analysis, corroborating the XRD evidence that indicated the existence of $CaCO_3$ in the fresh Ca catalyst. For all samples, three desorption temperature categories from weak, medium, and strong basic phases might be notable except 3Ca–1Ti and 3Ca–2Ti, which displayed only one area of CO_2 desorption. The CO_2-TPD pattern of 3Ca–1Ti and 3Ca–2Ti showed a small peak at 595 °C (0.06 mmol g^{-1}) and 647 °C (0.34 mmol g^{-1}), demonstrating that these two catalysts possess weak basic sites for CO_2. The stretched structure of oxygen atoms, which leads to destabilization of the 2p states on the surface oxygen ions, is thought to be the cause of the decrease in the specific intensity for 3Ca–1Ti and 3Ca–2Ti. The CaO content has OH^- (hydroxyl) groups in its composition (Petitjean et al., 2010), and as a result, for the 3Ca–1Ti and 3Ca–2Ti catalysts, the poor basic support sites can be the cause of the development of hydrogen carbonates, which results from a specific association between carbon dioxide and the weak basicity of OH^- bonds. The peaks at 135 °C for both Ca and 3Ca–3Ti catalysts might be because lattice oxygen in the Ca framework acts as a weak Lewis base, causing CO_2 desorption at low temperatures. Nichthima et al. (Dharmasaroja et al., 2020) indicated that the desorption peaks correspond to the Lewis acid-base pairing at this range. Simultaneously, two shoulders at 428 °C and 437 °C are ascribed to moderate unimodal desorption of CO_2. The addition of TNPs for the 3Ca–3Ti catalyst significantly increased the surface basicity of the catalyst with the highest CO_2 uptake (2.64 mmol g^{-1}). It also affected the spreading of the weak and strong basic sites. This increase in the population of the basic sites for the 3Ca–3Ti catalyst might be explained by the fact that Ca^{2+} ions (Papageridis et al., 2020) and Ti^{3+} sites (Xiong et al., 2012) increase the ionic density of the catalysts, thus enhancing the adsorption of CO_2 (polar molecule).

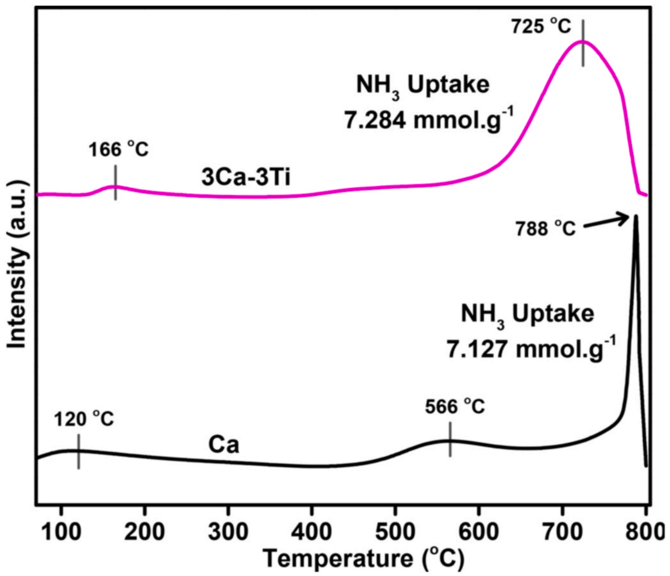

Fig. 9. Temperature-programmed desorption of NH_3 (NH_3-TPD) curves of the Ca and 3Ca–3Ti nanocatalysts.

The NH_3-TPD curves of the CaO–TiO_2 nanocatalysts present the acid strength and relative amount of acid sites, and the results are shown in Fig. 9 and quantified in Table 1. It is well understood that acidity is needed for the cleavage of *C*–O bonds. The CaO is an alkaline earth metal with comparatively high basicity capable of neutralizing acid sites by interaction with acid sites dispersed in catalyst supports, thereby causing a decline in the NH_3 uptake capacity. Only negligible acidity formation was observed for the 3Ca–1Ti and 3Ca–2Ti catalysts; therefore, the NH3-TPD pattern for those two samples is not shown here. The absence of acid sites for the 3Ca–1Ti and 3Ca–2Ti catalysts probably represented the NH_3 adsorption sites covered by the Ca^{2+} and resulted in the loss of the acid sites. Another reason for the acidity losses is the basic nature of CaO. Two desorption peaks for the 3Ca–3Ti sample were observed at 166 °C and 725 °C, which can be reasonably ascribed to the weak and strong acid sites. The propagation of an excess positive or negative charge caused by the formation of bridged hetero metal-oxygen bonds increased the acidic content of CaO after TNPs were introduced (Tanabe, 1970). The presence of Ca mterial cause to decrease the amount of Lewis acid sites (Xue et al., 2019), but the amount of NH_3-uptake for the Ca and 3Ca–3Ti catalysts is almost the same (7.127 mmol g^{-1} and 7.284 mmol g^{-1}) even though the Ca catalyst revealed a stronger acid site with a sharp peak at 788 °C. It is also renowned that the strong acid site of Ca encourages catalyst deactivation by coke deposition (Li et al., 2011). The conspicuous distinction suggests that the superior efficiency of the 3Ca–3Ti nanocatalyst may be due to the Brønsted acid sites on the catalyst. From the NH_3-TPD and CO_2-TPD profiles, we concluded that the bifunctional 3Ca–3Ti catalyst possesses both properties of basic and acidic sites, which is the main advantage for catalytic transesterification reactions.

The synthesized samples were characterized with the TEM technique to study their morphological and structural properties, and the result is shown in Fig. 10. It can be perceived that the uniform dispersion and coupling of TiO_2 nanoparticles, which is close to the spherical and rhombic-shaped anatase forms on the CaO nanorods, could be observed, indicating that TiO_2 nanoparticles and CaO nanorods are strongly chemically bonded. The average particle size of the TNPs and CaO is less than 100 nm, classifying them as nanoscale materials. The HRTEM images illustrate the lattice fringes of TiO_2 and CaO as 0.23 and 0.19 nm, respectively.

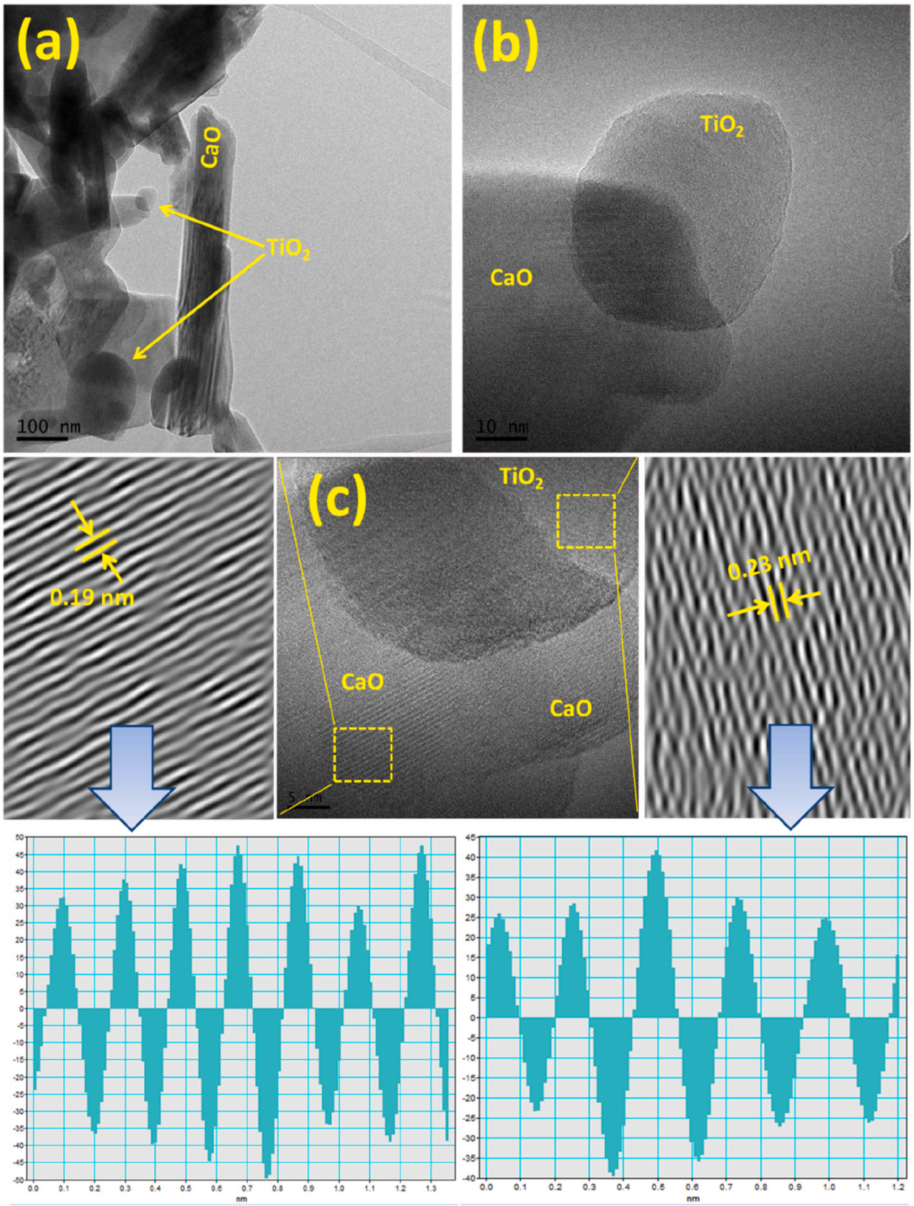

Fig. 10. (a) TEM images of 3Ca–3Ti nanocatalyst; (b) HRTEM images of 3Ca–3Ti nanocatalyst; (c) HRTEM image of the corresponding sample along with the d-spacing.

The nano-sized conduct of the catalysts is shown by selected area electron diffraction (SAED) obtained from the region shown in Fig. 11, which shows the presence of ring-like patterns that appear to be shaped in a spherical shape and well-defined diffraction points. Because the diffraction spots tend to be connected by a thin, ring-shaped band, the ring-like patterns indicated the existence of very tiny nanoclusters. Thus, the crystallite size measured from the XRD results was similar to the average particle sizes estimated by the TEM images. As a consequence, the TEM and XRD effects are highly correlated.

3.2. *Parametric influence on biodiesel yield*

Several tests were conducted at different reaction temperatures (50–90 °C) to study the influence of temperature on the transesterification reaction through CaO–TiO$_2$ nano-catalysts and dairy scum oil feedstock. The results are shown in Fig. 12. The initial dairy scum oil transesterification reaction was performed using 1 wt% catalyst and an oil to methanol ratio of 1:5. Temperatures of 50, 60, 70, 80, and 90 °C and a reaction time of 60 min were used. The reaction temperature can significantly influence the catalytic transesterification reaction, but no notable influence is seen on the biodiesel output in the absence of the catalyst. As presented in Fig. 12(a), it was discovered that the best biodiesel yield, 35.9%, was obtained when the reaction temperature was increased to 70 °C for the 3Ca–3Ti nanocatalyst. This mechanism may be clarified by increasing the temperature to the point that the catalyst and reactants collide more often, resulting in a faster reaction rate (Adenuga et al., 2020). Wenlei et al. (Xie et al., 2021) reported that the kinetic energy of the reactants developed as the temperature increased, causing them to collide more quickly with the higher reaction rate. However, a slight decrease in the biodiesel yield was observed when the reaction temperature was increased above 70 °C. The marginal reduction in the biodiesel yield as the reaction temperature increases may be ascribed to the improved viscosity of raw oil and the evaporation of methanol from the reaction medium, slowing the forward reaction rate and resulting in a lower biodiesel yield (Huang et al., 2021). This decreasing pattern was also observed in several experiments using various catalysts (Liu et al.,

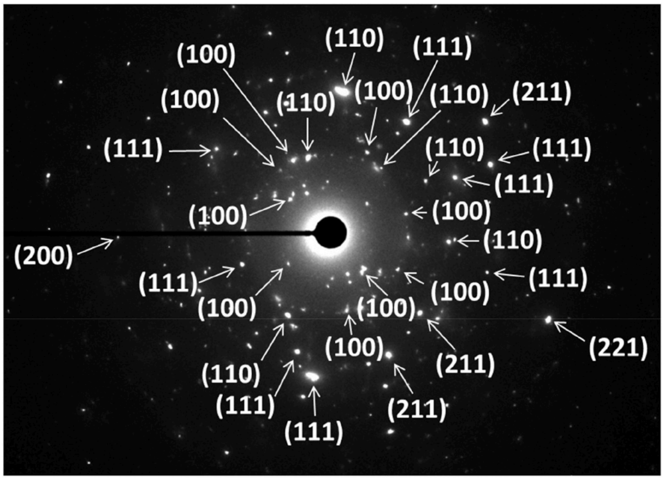

Fig. 11. SAED patterns of 3Ca–3Ti nano-sized catalysts.

2019; Kamran et al., 2020; Zhao et al., 2021). Besides, the superior performance of the 3Ca–3Ti nanocatalyst in the transesterification of dairy scum oil might be due to the disappearance of Ca–O and carbonate bonds, as shown in the FTIR analysis. Additionally, the pore size distribution patterns demonstrated that the 3Ca–3Ti sample shifted to smaller values (30–90 nm). Moreover, this catalyst exhibited bifunctionality, having both acid and basic sites, which facilitate the transesterification reaction. Furthermore, the significant interaction with the surface oxide of the 3Ca–3Ti nanocatalyst is attributed to Lewis acid sites. It can be assigned to the $\nu(\mathrm{COO}^-)$ mode of acetate, which could be the additional reason for its superior activity. Consequently, the optimal reaction temperature and the best catalyst for biodiesel processing were determined to be 70 °C and the 3Ca–3Ti nanocatalyst for the following optimization parameter.

In the transesterification reaction, the catalyst quantity is an essential determining parameter. By holding the other parameters such as temperature (70 °C), oil to methanol ratio (1:5), and pressure (100 kpa) unchanged, the amount of catalyst added to the dairy scum oil was measured as a percentage of weight and ranged from 1 wt% to 5 wt%. The reaction time was also varied from 60 to 300 min to maximize the reaction time for an optimal biodiesel yield. The biodiesel production versus the ratio percent of catalyst loading and reaction time are displayed in Fig. 12 (b). The biodiesel yield increased from 52.90% to 59.80% by increasing the time from 60 to 120 min, but there was a minor change in the yield from 59.80% to 60.10% from 120 to 300 min. Therefore, the above observations imply that the acid-base catalyst is sufficiently active within the first 120 min of the transesterification reaction. As a result, 120 min was chosen as the optimum transesterification period for the optimal biodiesel yield. In the transesterification of dairy scum oil, 59.80% biodiesel yield occurs after 120 min of the reaction period and 3 wt% of optimum catalyst loading. A further increase in the catalyst did not noticeably influence the biodiesel yield. This may be because the small volume of catalyst used to turn dairy scum oil into fatty acid methyl ester is inadequate. If the volume of the catalyst increases in the transesterification, the viscosity of the mixture increases, resulting in fewer possible interactions between the catalyst and the methanol reagents, causing the biodiesel yield to decrease (Saba et al., 2016). Therefore, an optimum condition of 3 wt% catalyst and 120 min reaction time was assumed to lead to the optimum conversion of dairy scum oil to biodiesel (59.80%).

The volume of methanol used in the biodiesel production method, also known as the "dairy scum oil to methanol molar ratio", is critical for increasing the biodiesel yield. The type of catalyst has the most significant impact on this ratio (Ting et al., 2008; Chang et al., 2013). Besides, because the temperature is directly proportional to the pressure in gaseous systems, it is suggested that increasing pressure above ambient pressure decreases the temperature demand of a reacting liquid system like that of biodiesel processing. As a result, the amount of energy needed to increase the temperature of the responding masses is reduced. Temperature is inversely proportional to pressure if other factors are held at optimal levels. In this part of the investigation, the effect of the oil to methanol molar ratio and the pressure on the biodiesel generation

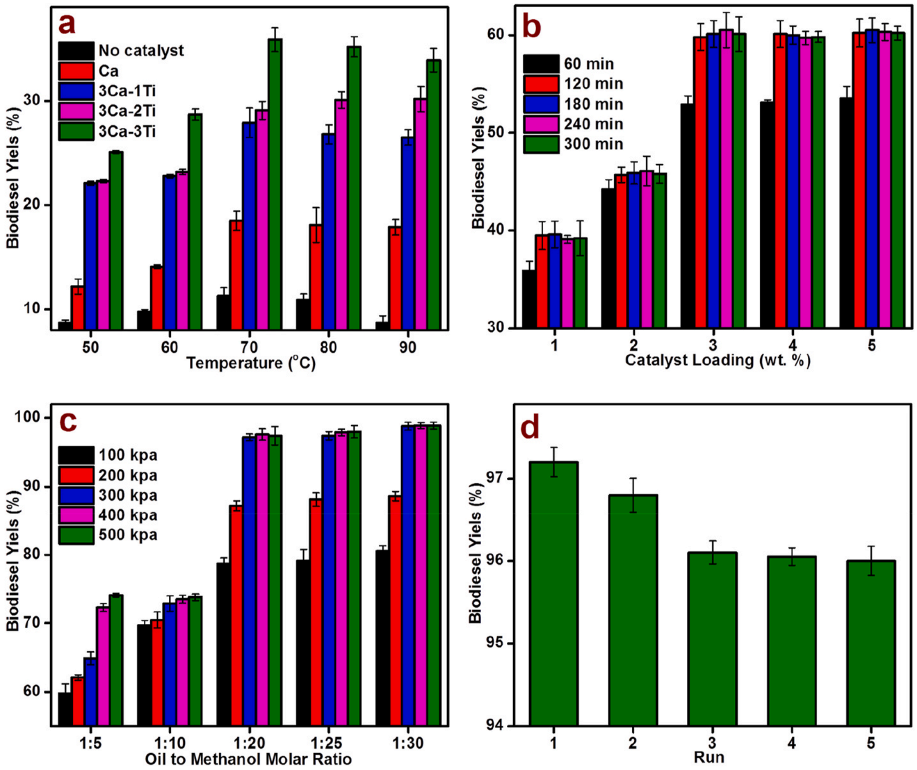

Fig. 12. Evolution of the biodiesel yield as a function of (a) different catalysts and temperature (catalyst: 1 wt%, pressure: 100 kPa, oil to methanol ratio: 1:5, reaction time: 60 min); (b) catalyst loading and reaction time (catalyst: 3Ca:3Ti, temperature: 70 °C, oil to methanol ratio: 1:5, pressure: 100 kPa); (c) pressure and oil to methanol ratio (catalyst: 3Ca:3Ti, temperature: 70 °C, catalyst loading: 3 wt%, reaction time: 120 min); (d) reusability effect of catalyst on the FAMEs yield (catalyst: 3Ca:3Ti, temperature: 70 °C, catalyst loading: 3 wt%, reaction time: 120 min, oil to methanol ratio: 1:20, pressure: 300 kPa) [error bars equal 95% confidence interval (CI)].

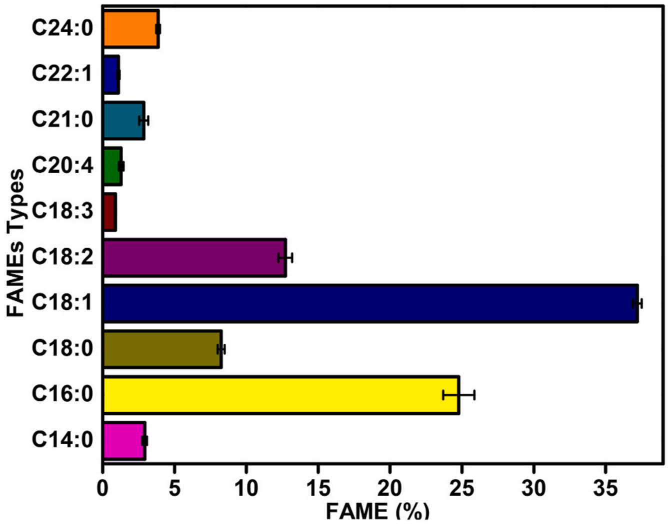

Fig. 13. FAMEs composition of the dairy scum oil biodiesel product [error bars equal 95% confidence interval (CI)].

yield is investigated in the range of 1:5 to 1:30 and 100 kPa–500 kPa, as depicted in Fig. 12 (c), while keeping the other parameters such as temperature (70 °C), 3Ca:3Ti catalyst rate (3 wt%), and reaction time (120 min) constant. Flooding can occur in the reaction phase due to the high methanol ratio, diluting the active sites. Furthermore, the flooded methanol induced soap emulsion between layers, which hindered the separation method, increased production costs (Madhu and Sharma, 2017). Thus, one of the essential parameters to maximize the biodiesel yield is the methanol to oil molar ratio. The result illustrated that it is possible to reach a biodiesel yield of more than 97 wt% with a 1:20 oil to methanol ratio for 300 kPa, while a further increase gives almost similar results, as the excess methanol diluted the reaction solution; thus, the efficiency of the interaction between the reactant molecules decreases (Changmai et al., 2021). Because a higher ratio of methanol promotes the solubility of glycerol, the separation of biodiesel from glycerol is more challenging (Lim et al., 2009). Therefore, a 1:20 oil to methanol ratio was the optimum ratio in this study. The tests revealed that pressure significantly impacts the biodiesel yield in the pressure range of 100–300 kPa. The boiling point of methanol increased as the pressure increased. This enabled the methanol to remain liquid during the reaction. If the pressure was increased, the number of molecules per volume unit increased significantly, resulting in further interactions. This aided the development of the reaction even further. The findings show that over such intensity levels, pressure has a significant impact on the biodiesel yield. However, after 300 kPa, no variations in the biodiesel yield were observed because the reacting system had reached equilibrium. Because the reverse backward reaction could not be inhibited at pressures greater than 300 kPa, more dairy scum oil remained in the reaction, but at pressures lower than 300 kPa, the forward reaction dominated the reversible reaction with constant elimination of methanol. Therefore, the biodiesel yield remains almost constant beyond 300 kPa. To conclude the aforementioned analysis, the optimum condition to achieve a biodiesel yield of 97.20% is 3 wt% 3Ca:3Ti nanocatalyst, 70 °C temperature, 120 min reaction time, 1:20 oil to methanol ratio, and 300 kPa pressure.

The durability and reusability of a heterogeneous catalyst are critical for feasible transesterification processes. After transesterifying dairy scum oil, the catalyst was extracted using filter paper. The surface was cleaned with methanol on a hot plate to clear any remaining oil. In order to burn any organic deposits and regenerate the active sites in the surface, the catalyst was dried overnight and calcined for 3 h at 800 °C. Fig. 12 (d) shows the biodiesel yield of the 3Ca:3Ti nanocatalyst catalyzed dairy scum oil transesterification in five cycles. Experiments were conducted with 3 wt% 3Ca:3Ti nanocatalyst, 70 °C temperature, 120 min reaction time, 1:20 oil to methanol ratio, and 300 kPa pressure. The findings indicate that even after five cycles, the biodiesel yield decreased marginally from 97.20% to 96%, a decrease of only 1.20%. The catalyst particles could have agglomerated after being reused for transesterification, resulting in a decreased catalyst operation. If the number of transesterification cycles increased, the scale of the agglomeration of catalyst particles became larger. As a result, as the amount of cycles grows, the biodiesel yield decreases. Following an initial decrease in the catalytic efficiency between the first and third catalytic runs, the obtained yield remains relatively steady from then on. With just a slight loss of catalytic activity, the 3Ca:3Ti nanocatalyst has a strong potential for reusability in the transesterification reaction for biodiesel processing.

Table 3
Physical and chemical properties of dairy scum biodiesel and diesel and methods used for their determination.

Properties	Units	Method	Obtained values (Biodiesel)	Diesel	EN14214 (Accepted limits)
Cloud point	°C	ASTM D2500	4 ± 0.20	−15 to 5	−3 to 12
Flash point	°C	ASTM D93	137 ± 6.80	54	>120
Kinematic viscosity @ 40 °C	$mm^2.s^{-1}$	ASTM D445	2.79 ± 0.34	2.54	3.5 to 5.0
Density @ 15 °C	$kg.m^{-3}$	Density meter	879 ± 43	832.6	860–900
Cetane number	min	ASTM D6890	53 ± 2.60	45–55	>51
Sulphur content	wt.%	Multi EA 5000	0.01 ± 0.0005	0.009	<10
Ash content	wt.%	ASTM D874	Nil	0.08	<0.02

The composition of FAMEs of dairy scum oil biodiesel is analyzed via the GC–MS method and is presented in Fig. 13. The physical properties are within the EN14214 standards, as displayed in Table 3. The total FAME content of dairy scum oil biodiesel was 95.85%, indicating the high purity of the biodiesel. Oleic acid (C18:1) was the most abundant FAME in dairy scum oil biodiesel, with a 37.2% content. It was apparent that the dairy scum oil was detected with the presence of 14.89% polyunsaturated fatty acids (linoleic (C18:2), linolenic (C18:3), arachidonic (C20:4 ω6)), 38.29% monosaturated fatty acids (oleic (C18:1), erucic acid (C22:1)), and 42.67% fatty acids (myristic acid (C14:0), palmitoleic acid (C16:0), stearic acid (C18:0), heneicosanoic acid (C21:0), and lignoceric acid (C24:0)). The most significant factor that influences the fluidity of the biodiesel is its viscosity. As shown in Table 3, the assessed viscosity (2.79 $mm^2 s^{-1}$) of the biodiesel is within the acceptable limit, and it is suggestively lower than the viscosity of the biodiesel achieved in the previous work that used rhodococcus opacus (Goswami et al., 2017), sterculia foetida and jatropha curcas methyl ester (Ong et al., 2013), and calophyllum inophyllum (Ong et al., 2014). Low viscosity is advantageous because it produces high flow properties, a high atomization efficiency, drop rate, and fuel penetration capacity (Goswami et al., 2017). The flashpoint was 137 °C, which is higher than the flashpoint of petroleum diesel. Because of the higher flash point, storage and transportation problems are less of a concern (Krawczyk, 1996; Wardle, 2003). The collected biodiesel had a density of 879 kg m^{-3}. The fuel density affects exhaust pollution, with high-density fuel causing a rise in a specific matter and NO_x emissions (Canakci and Sanli, 2008). In general, biodiesel fuel has a slightly higher density than diesel fuel (Ong et al., 2014). The cloud point and flash pour point of dairy scum oil biodiesel satisfy the standard limitation of biodiesel. Besides, the cetane number is a crucial characteristic of methyl ester that affects the ignition delay. It can be described as the fuel's capacity to self-ignite quickly after being injected. Biodiesel generally has a higher cetane

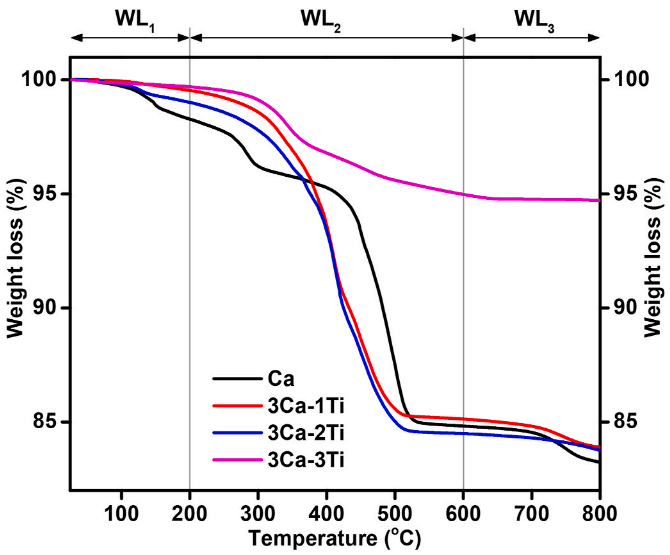

Fig. 14. TGA curves of the used nanostructured catalysts.

number than petroleum diesel (Demirbaş, 2003). The cetane number decreases with decreasing chain length and increasing branching (Georgogianni et al., 2007). The acceptable cetane number of the biodiesel (53) is because of the current research's high saturated fatty acid content in the dairy scum oil. The existence of the above fatty acid compositions made it an effective green energy source for biodiesel processing, and the quality of the produced biodiesel under optimal conditions is in the range of EN14214 standards.

3.3. Used nanocatalyst characterization

To evaluate the thermal stability of the CaO–TiO_2 nanocatalysts, TGA analysis was performed, and the results are shown in Fig. 14. The quantity of placed coke, weight losses, carbon contents, and used catalyst surface area are reported in Table 4. The catalyst could be quickly separated from the reaction mixture after the transesterification processes through filtration, and the 3Ca–3Ti nanocatalyst displayed no deactivation after several recycles. As shown in the figure, the weight loss first (WL_1) occurred between 27 °C and 200 °C, while major decomposition also occurred at around 200 °C–600 °C (WL_2) and above 600 °C (WL_3). WL_1 is attributed to the mass loss due to water loss in the structure, WL_2 is attributed to the oxidation of the organic structure, and WL_3 is attributed to the oxidation of more stable deposited coke. In the temperature range of 200–600 °C, the Ca, 3Ca–1Ti, 3Ca–2Ti, and 3Ca–3Ti nanocatalyst showed a weight loss of 13.45 wt%, 14.41 wt%, 14.52 wt%, and 4.72 wt%, respectively, which may be due to degradation of the structure of the material mentioned above. At 600 °C, the decomposition was complete, and the weight of the catalyst remained almost constant, suggesting that 600 °C should be the maximum calcination temperature for the CaO produced from organic ash over the TNP nanocatalyst. The 3Ca–3Ti nanocatalyst was highly stable with the least total weight loss of 5.28%, a carbon content of 10.30%, and the difference between surface areas of 1.53, whereas the first three catalysts have inferior thermal stability. As seen in the FTIR analysis, this high stability might be attributed to the disappearance of Ca–O and carbonate bonds and the formation of acetylide in the 3Ca–3Ti nanocatalyst.

4. Conclusions

The use of a straightforward, inexpensive, and easy method for synthesizing CaO nanomaterials derived from organic ash over TNPs in the large-scale development of biodiesel was the standout feature of the present study. The optimum ratio of CaO to TNPs is 3:3, and the highest catalytic activity was obtained over the corresponding catalyst. The 3Ca–3Ti nanocatalyst demonstrated superior performance for transesterification. In comparison to the TPD analysis of the catalysts, it was shown that the 3Ca–3Ti nanocatalyst exhibited bifunctionality, having both acid and basic sites. In addition, TNPs are attributed to Lewis acid sites and can be assigned to the $\nu(COO^-)$ mode of acetate, indicating a significant interaction with the surface oxide. The disappearance of Ca–O and carbonate bonds and the formation of acetylide for the 3Ca–3Ti nanocatalysts can be seen in the FTIR spectrum. The maximum biodiesel yield was 97.2%, which was obtained under the settings of 3 wt% 3Ca:3Ti nanocatalyst, 70 °C temperature, 120 min reaction time, 1:20 oil to methanol ratio, and 300 kPa pressure. The reusability test showed that the synthesized 3Ca–3Ti nanocatalyst is reusable for up to five runs with negligible activity loss. Moreover, the main properties of the biodiesel products were determined to be consistent with EN 14214 standards. The current study offers a low-cost and environmentally friendly process to synthesize metal-free catalysts such as CaO obtained from organic ash over TNPs.

Large-scale refining for the desired end product(s) and exemplary catalyst stability have always been essential for economic sustainability. However, another issue with CaO-derived catalysts is that they tend to attach to glycerol throughout the process, and the resulting Ca-glycerol complex is less catalytically active than CaO. Therefore, further research and the use of novel characterization methods for the used catalysts, such as XRF, XPS, and SEM, are promising in terms of future experimental approaches to obtain a detailed understanding of the produced coke. In addition, a modification by doping non-precious active metals and a combination of the catalyst synthesis methods are suggested to enhance the performance of waste-derived heterogeneous catalysts.

Author agreement statement

Author Contributions Statement. Walid Nabgan Writing - original draft Agreed. Bahador Nabgan Analysis Agreed. Muhammad Ikram Writing and characterization Agreed. Arvind H. Jadhav Characterization Agreed. Mohamad Wijayanuddin Ali Funding acquisition Agreed. Anwar Ul-Hamid Writing - review and editing Agreed. Hyungseok Nam Writing - review and editing Agreed. Parashuram Lakshminarayana Methodology Agreed. Ankit kumar Revision and paraphrasing Agreed. Mahadi B. Bahari Revision Agreed. Nur Farahain Khusnun Revision and methodology Agreed.

Declaration of competing interest

The authors declare that they have no known competing financial interests or personal relationships that could have appeared to influence

Table 4
Weight loss, carbon content, and surface area of the used catalysts.

Catalysts	Weight loss (%)			Total weight loss (%)	Carbon Content (wt.%)	Fresh catalyst Surface area ($m^2.g^{-1}$)^a	Spent catalyst Surface area ($m^2.g^{-1}$)^b	Difference between surface area (a-b)
	WL_1	WL_2	WL_3					
Ca	1.72	13.45	1.60	16.77	29.7	5.99	2.12	3.87
3Ca–1Ti	0.46	14.41	1.22	16.09	31.4	22.76	14.10	8.66
3Ca–2Ti	0.99	14.52	0.72	16.23	28.2	15.21	5.60	9.61
3Ca–3Ti	0.30	4.72	0.26	5.28	10.3	7.93	6.40	1.53

the work reported in this paper.

Acknowledgments

The principal author, Walid Nabgan, is thankful for Universiti Teknologi Malaysia's support in the form of the Post-Doctoral Fellowship Scheme "Simultaneous heavy metals ions and organic pollutants photoredox reactions over SiO_2/ZrO_2 based catalysts under solar-light irradiation" (PDRU Grant number: 05E49). In addition, the authors acknowledge the financial support given for this work by Universiti Teknologi Malaysia (UTM) under the Collaborative Research Grant (CRG) numbers 07G61, 07G59, and 07G62 and the University Laboratory Management Unit (UPMU).

References

Abdullah, R.F., Rashid, U., Hazmi, B., Ibrahim, M.L., Tsubota, T., Alharthi, F.A., 2022. Potential heterogeneous nano-catalyst via integrating hydrothermal carbonization for biodiesel production using waste cooking oil. Chemosphere 286, 131913.

Adenuga, A.A., Idowu, O.O., Oyekunle, J.A.O., 2020. Synthesis of quality biodiesel from Calophyllum inophyllum kernels through reactive extraction method: optimization of process parameters and characterization of the products. Renew. Energy 145, 2530–2537.

Ahmed, M.H., Byrne, J.A., McLaughlin, J., Ahmed, W., 2013. Study of human serum albumin adsorption and conformational change on DLC and silicon doped DLC using XPS and FTIR spectroscopy. J. Biomaterials Nanobiotechnol. .04No.02, 10.

Amini, Z., Ilham, Z., Ong, H.C., Mazaheri, H., Chen, W.-H., 2017. State of the art and prospective of lipase-catalyzed transesterification reaction for biodiesel production. Energy Convers. Manag. 141, 339–353.

Barabás, I., Todoruţ, I.-A., 2011. Biodiesel quality, standards and properties. Biodiesel Qual. Emissions by-products 3–28.

Behera, A.R., Dutta, K., Verma, P., Daverey, A., Sahoo, D.K., 2019. High lipid accumulating bacteria isolated from dairy effluent scum grown on dairy wastewater as potential biodiesel feedstock. J. Environ. Manag. 252, 109686.

Bellido, J.D.A., De Souza, J.E., M'Peko, J.-C., Assaf, E.M., 2009. Effect of adding CaO to ZrO2 support on nickel catalyst activity in dry reforming of methane. Appl. Catal. Gen. 358, 215–223.

Canakci, M., Sanli, H., 2008. Biodiesel production from various feedstocks and their effects on the fuel properties. J. Ind. Microbiol. Biotechnol. 35, 431–441.

Cao, N., Zhang, Y., 2015. Study of reduced graphene oxide preparation by Hummers' method and related characterization. J. Nanomater. 2015, 168125.

Carlucci, C., Degennaro, L., Luisi, R., 2019. Titanium dioxide as a catalyst in biodiesel production. Catalysts 9.

Chang, B., Fu, J., Tian, Y., Dong, X., 2013. Soft-template synthesis of sulfonated mesoporous carbon with high catalytic activity for biodiesel production. RSC Adv. 3, 1987–1994.

Changmai, B., Rano, R., Vanlalveni, C., Rokhum, L., 2021. A novel Citrus sinensis peel ash coated magnetic nanoparticles as an easily recoverable solid catalyst for biodiesel production. Fuel 286, 119447.

Channappagoudra, M., 2021. Effect of copper oxide nanoadditive on diesel engine performance operated with dairy scum biodiesel. Int. J. Ambient Energy 42, 530–539.

Daroughegi Mofrad, B., Hayati-Ashtiani, M., Rezaei, M., 2018. Preparation of pillared nanoporous bentonite and its application as catalyst support in dry reforming reaction. Asia Pac. J. Chem. Eng. 13, e2188.

Dawood, S., Koyande, A.K., Ahmad, M., Mubashir, M., Asif, S., Klemeš, J.J., Bokhari, A., Saqib, S., Lee, M., Qyyum, M.A., Show, P.L., 2021. Synthesis of biodiesel from non-edible (Brachychiton populneus) oil in the presence of nickel oxide nanocatalyst: parametric and optimisation studies. Chemosphere 278, 130469.

Dehghani, S., Haghighi, M., Vardast, N., 2019. Structural/texture evolution of CaO/MCM-41 nanocatalyst by doping various amounts of cerium for active and stable catalyst: biodiesel production from waste vegetable cooking oil. Int. J. Energy Res. 43, 3779–3793.

Demirbaş, A., 2003. Biodiesel fuels from vegetable oils via catalytic and non-catalytic supercritical alcohol transesterifications and other methods: a survey. Energy Convers. Manag. 44, 2093–2109.

Deyab, M.A., Hamdi, N., Lachkar, M., Bali, B.E., 2018. Clay/Phosphate/Epoxy nanocomposites for enhanced coating activity towards corrosion resistance. Prog. Org. Coating 123, 232–237.

Dharmasaroja, N., Ratana, T., Tungkamani, S., Sornchamni, T., Simakov, D.S.A., Phongaksorn, M., 2020. CO2 Reforming of Methane over the Growth of Hierarchical Ni nanosheets/Al2O3-MgO Synthesized via the Ammonia Vapour Diffusion Impregnation. The Canadian Journal of Chemical Engineering n/a.

Durdu, S., 2019. Characterization and Investigation of Biological Properties of Ag-Doped TiO2 Coatings Fabricated on Titanium, vol. 20. Eskişehir Technical University Journal of Science and Technology A-Applied Sciences and Engineering, pp. 17–33.

Georgogianni, K.G., Kontominas, M.G., Tegou, E., Avlonitis, D., Gergis, V., 2007. Biodiesel production:reaction and process parameters of alkali -catalyzed transesterification of waste frying oils. Energy Fuel. 21, 3023–3027.

Goswami, L., Tejas Namboodiri, M.M., Vinoth Kumar, R., Pakshirajan, K., Pugazhenthi, G., 2017. Biodiesel production potential of oleaginous Rhodococcus opacus grown on biomass gasification wastewater. Renew. Energy 105, 400–406.

Hadiyanto, H., Lestari, S.P., Abdullah, A., Widayat, W., Sutanto, H., 2016. The development of fly ash-supported CaO derived from mollusk shell of Anadara granosa and Paphia undulata as heterogeneous CaO catalyst in biodiesel synthesis. Int. J. Energy Environ. Eng. 7, 297–305.

Hasan, M.A., Zaki, M.I., Pasupulety, L., 2003. Oxide-catalyzed conversion of acetic acid into acetone: an FTIR spectroscopic investigation. Appl. Catal. Gen. 243, 81–92.

Helmi, M., Tahvildari, K., Hemmati, A., Aberoomand azar, P., Safekordi, A., 2021. Phosphomolybdic acid/graphene oxide as novel green catalyst using for biodiesel production from waste cooking oil via electrolysis method: optimization using with response surface methodology (RSM). Fuel 287, 119528.

Ho, W.W.S., Ng, H.K., Gan, S., Tan, S.H., 2014. Evaluation of palm oil mill fly ash supported calcium oxide as a heterogeneous base catalyst in biodiesel synthesis from crude palm oil. Energy Convers. Manag. 88, 1167–1178.

Huang, J., Zou, Y., Yaseen, M., Qu, H., He, R., Tong, Z., 2021. Fabrication of hollow cage-like CaO catalyst for the enhanced biodiesel production via transesterification of soybean oil and methanol. Fuel 290, 119799.

Kamran, E., Mashhadi, H., Mohammadi, A., Ghobadian, B., 2020. Biodiesel production from Elaeagnus angustifolia.L seed as a novel waste feedstock using potassium hydroxide catalyst. Biocatal. Agric. Biotechnol. 25, 101578.

Khaligh, N.G., Mihankhah, T., Shahnavaz, Z., Zaharani, L., Johan, M.R., 2021. Solar energy and TiO2 nanotubes: biodiesel production from waste cooking olive oil. Environ. Prog. Sustain. Energy 40, e13537.

Kochan, K., Heraud, P., Kiupel, M., Yuzbasiyan-Gurkan, V., McNaughton, D., Baranska, M., Wood, B.R., 2015. Comparison of FTIR transmission and transfection substrates for canine liver cancer detection. Analyst 140, 2402–2411.

Kouzu, M., Yamanaka, S.-y., Hidaka, J.-s., Tsunomori, M., 2009. Heterogeneous catalysis of calcium oxide used for transesterification of soybean oil with refluxing methanol. Appl. Catal. Gen. 355, 94–99.

Krawczyk, T., 1996. Biodiesel-alternative fuel makes inroads but hurdles remain. inform 7, 801–815.

Krim, L., Prot, C., Alikhani, E.l.M., Manceron, L., 2000. Reactions of ground state Ti atoms with NO: insertion versus complexation. An IR matrix isolation study. Chem. Phys. 254, 267–274.

Krishnamurthy, K.N., Sridhara, S.N., Ananda Kumar, C.S., 2020. Optimization and kinetic study of biodiesel production from Hydnocarpus wightiana oil and dairy waste scum using snail shell CaO nano catalyst. Renew. Energy 146, 280–296.

Li, B., Cao, H., 2011. ZnO@graphene composite with enhanced performance for the removal of dye from water. J. Mater. Chem. 21, 3346–3349.

Li, Q., Sui, Z., Zhou, X., Zhu, Y., Zhou, J., Chen, D., 2011. Coke formation on Pt–Sn/Al2O3 catalyst in propane dehydrogenation: coke characterization and kinetic study. Top. Catal. 54, 888.

Lim, B.P., Maniam, G.P., Hamid, S., 2009. Biodiesel from adsorbed waste oil on spent bleaching clay using CaO as a heterogeneous catalyst. Eur. J. Sci. Res. 33, 347–357.

Liu, J.-Z., Cui, Q., Kang, Y.-F., Meng, Y., Gao, M.-Z., Efferth, T., Fu, Y.-J., 2019. Euonymus maackii Rupr. Seed oil as a new potential non-edible feedstock for biodiesel. Renew. Energy 133, 261–267.

Madhu, D., Sharma, Y.C., 2017. Synthesis of a reusable novel catalyst (β-tricalcium phosphate) for biodiesel production from a common Indian tribal feedstock. Resour. Effic. Technol. 3, 144–157.

Marinković, D.M., Avramović, J.M., Stanković, M.V., Stamenković, O.S., Jovanović, D.M., Veljković, V.B., 2017. Synthesis and characterization of spherically-shaped CaO/γ-Al2O3 catalyst and its application in biodiesel production. Energy Convers. Manag. 144, 399–413.

Meng, X., Che, C., Zhang, J., Gong, Z., Si, M., Yang, G., Cao, L., Liu, J., 2019. Structural characterization and immunomodulating activities of polysaccharides from a newly collected wild Morchella sextelata. Int. J. Biol. Macromol. 129, 608–614.

Mines, U.S.B.o., 1955. Report of Investigations. U.S. Department of the Interior, Bureau of Mines.

Mofijur, M., Siddiki, S.Y.A., Shuvho, M.B.A., Djavanroodi, F., Fattah, I.M.R., Ong, H.C., Chowdhury, M.A., Mahlia, T.M.I., 2021. Effect of nanocatalysts on the transesterification reaction of first, second and third generation biodiesel sources- A mini-review. Chemosphere 270, 128642.

Nabgan, B., Nabgan, W., Tuan Abdullah, T.A., Tahir, M., Gambo, Y., Ibrahim, M., Syie Luing, W., 2017a. Parametric study on the steam reforming of phenol-PET solution to hydrogen production over Ni promoted on Al2O3-La2O3 catalyst. Energy Convers. Manag. 142, 127–142.

Nabgan, B., Tahir, M., Abdullah, T.A.T., Nabgan, W., Gambo, Y., Mat, R., Saeh, I., 2017b. Ni/Pd-promoted Al2O3–La2O3 catalyst for hydrogen production from polyethylene terephthalate waste via steam reforming. Int. J. Hydrogen Energy 42, 10708–10721.

Nabgan, W., Nabgan, B., Tuan Abdullah, T.A., Alqaraghuli, H., Ngadi, N., Jalil, A.A., Othman, B.M., Ibrahim, A.M., Siang, T.J., 2020. Ni–Pt/Al nano-sized catalyst supported on TNPs for hydrogen and valuable fuel production from the steam reforming of plastic waste dissolved in phenol. Int. J. Hydrogen Energy 45, 22817–22832.

Nabgan, W., Nabgan, B., Tuan Abdullah, T.A., Jalil, A.A., Ul-Hamid, A., Ikram, M., Nordin, A.H., Coelho, A., 2021. Production of hydrogen and valuable fuels from polyethylene terephthalate waste dissolved in phenol reforming and cracking reactions via Ni-Co/CeO2 nano-catalyst. J. Anal. Appl. Pyrol. 154, 105018.

Nabgan, W., Tuan Abdullah, T.A., Mat, R., Nabgan, B., Gambo, Y., Moghadamian, K., 2016a. Acetic acid-phenol steam reforming for hydrogen production: effect of different composition of La2O3-Al2O3 support for bimetallic Ni-Co catalyst. J. Environ. Chem. Eng. 4, 2765–2773.

Nabgan, W., Tuan Abdullah, T.A., Mat, R., Nabgan, B., Gambo, Y., Triwahyono, S., 2016b. Influence of Ni to Co ratio supported on ZrO2 catalysts in phenol steam reforming for hydrogen production. Int. J. Hydrogen Energy 41, 22922–22931.

Ong, H.C., Masjuki, H.H., Mahlia, T.M.I., Silitonga, A.S., Chong, W.T., Leong, K.Y., 2014. Optimization of biodiesel production and engine performance from high free fatty acid Calophyllum inophyllum oil in CI diesel engine. Energy Convers. Manag. 81, 30–40.

Ong, H.C., Silitonga, A.S., Masjuki, H.H., Mahlia, T.M.I., Chong, W.T., Boosroh, M.H., 2013. Production and comparative fuel properties of biodiesel from non-edible oils: jatropha curcas, Sterculia foetida and Ceiba pentandra. Energy Convers. Manag. 73, 245–255.

Ong, H.C., Tiong, Y.W., Goh, B.H.H., Gan, Y.Y., Mofijur, M., Fattah, I.M.R., Chong, C.T., Alam, M.A., Lee, H.V., Silitonga, A.S., Mahlia, T.M.I., 2021. Recent advances in biodiesel production from agricultural products and microalgae using ionic liquids: opportunities and challenges. Energy Convers. Manag. 228, 113647.

Papageridis, K.N., Charisiou, N.D., Douvartzides, S., Sebastian, V., Hinder, S.J., Baker, M. A., AlKhoori, S., Polychronopoulou, K., Goula, M.A., 2020. Promoting effect of CaO-MgO mixed oxide on Ni/γ-Al2O3 catalyst for selective catalytic deoxygenation of palm oil. Renew. Energy 162, 1793–1810.

Pavlović, S.M., Marinković, D.M., Kostić, M.D., Janković-Častvan, I.M., Mojović, L.V., Stanković, M.V., Veljković, V.B., 2020. A CaO/zeolite-based catalyst obtained from waste chicken eggshell and coal fly ash for biodiesel production. Fuel 267, 117171.

Petitjean, H., Chizallet, C., Krafft, J.-M., Che, M., Lauron-Pernot, H., Costentin, G., 2010. Basic reactivity of CaO: investigating active sites under operating conditions. Phys. Chem. Chem. Phys. 12, 14740–14748.

Saba, T., Estephane, J., El Khoury, B., El Khoury, M., Khazma, M., El Zakhem, H., Aouad, S., 2016. Biodiesel production from refined sunflower vegetable oil over KOH/ZSM5 catalysts. Renew. Energy 90, 301–306.

Sagar, N.A., Pareek, S., Sharma, S., Yahia, E.M., Lobo, M.G., 2018. Fruit and vegetable waste: bioactive compounds, their extraction, and possible utilization. Compr. Rev. Food Sci. Food Saf. 17, 512–531.

Son, E.K., Yeom, S.H., 2021. Repeated biodiesel production using a cartridge containing solid catalysts manufactured from waste scallop shells for simultaneous lipid extraction and transesterification process. Biotechnol. Bioproc. Eng. 26, 145–155.

Soudagar, M.E.M., Nik-Ghazali, N.-N., Kalam, M.A., Badruddin, I.A., Banapurmath, N.R., Yunus Khan, T.M., Bashir, M.N., Akram, N., Farade, R., Afzal, A., 2019. The effects of graphene oxide nanoparticle additive stably dispersed in dairy scum oil biodiesel-diesel fuel blend on CI engine: performance, emission and combustion characteristics. Fuel 257, 116015.

Srikanth, H.V., Venkatesh, J., Godiganur, S., Manne, B., Bharath Kumar, S., Spurthy, S., 2020. Combustion, performance, and emission characteristics of dairy-washed milk scum biodiesel in a dual cylinder compression ignition engine. Energy Sources, Part A Recovery, Util. Environ. Eff. 42, 2873–2890.

Srikanth, H.V., Venkatesh, J., Godiganur, S., Venkateswaran, S., Manne, B., 2017. Bio-based diluents improve cold flow properties of dairy washed milk-scum biodiesel. Renew. Energy 111, 168–174.

Tanabe, K., 1970. Chapter 4 - acid and base centres: their structure and acid-base properties. In: Tanabe, K. (Ed.), Solid Acids and Bases. Academic Press, pp. 45–101.

Thangarasu, V., Anand, R., 2019. Chapter 17 - comparative evaluation of corrosion behavior of Aegle Marmelos Correa diesel, biodiesel, and their blends on aluminum and mild steel metals. In: Azad, A.K., Rasul, M. (Eds.), Advanced Biofuels. Woodhead Publishing, pp. 443–471.

Ting, W.-J., Huang, C.-M., Giridhar, N., Wu, W.-T., 2008. An enzymatic/acid-catalyzed hybrid process for biodiesel production from soybean oil. J. Chin. Inst. Chem. Eng. 39, 203–210.

Waheed, A., Wang, X., Maeda, N., Naito, S., Baiker, A., 2019. Surface processes occurring during aqueous phase ethanol reforming on Ru/TiO2 tracked by ATR-IR spectroscopy. Appl. Catal. Gen. 581, 111–115.

Wakabayashi, F., Kondo, J.N., Domen, K., Hirose, C., 1997. FT-IR study of the interaction of oxygen, argon, helium, nitrogen and xenon with hydroxyl groups in H-Y zeolite at low temperatures. Microporous Mater. 8, 29–37.

Wardle, D.A., 2003. Global Sale of Green Air Travel Supported Using biodiesel11A Web Page Devoted to This Topic Will Be Maintained at, vol. 7. Renewable and Sustainable Energy Reviews, pp. 1–64. http://www.phy.auckland.ac.nz/staff/daw.

Xie, W., Gao, C., Li, J., 2021. Sustainable biodiesel production from low-quantity oils utilizing H6PV3MoW8O40 supported on magnetic Fe3O4/ZIF-8 composites. Renew. Energy 168, 927–937.

Xiong, L.-B., Li, J.-L., Yang, B., Yu, Y., 2012. Ti3+ in the surface of titanium dioxide: generation, properties and photocatalytic application. J. Nanomater. 2012, 831524.

Xue, H., Meng, T., Liu, F., Guo, X., Wang, S., Mao, D., 2019. Enhanced resistance to calcium poisoning on Zr-modified Cu/ZSM-5 catalysts for the selective catalytic reduction of NO with NH3. RSC Adv. 9, 38477–38485.

Yatish, K.V., Lalithamba, H.S., Suresh, R., Dayananda, G.N., 2018. Sodium phosphate synthesis through glycerol purification and its utilization for biodiesel production from dairy scum oil to economize production cost. Sustain. Energy Fuel. 2, 1299–1304.

Yusuff, A.S., Gbadamosi, A.O., Popoola, L.T., 2021. Biodiesel production from transesterified waste cooking oil by zinc-modified anthill catalyst: parametric optimization and biodiesel properties improvement. J. Environ. Chem. Eng. 9, 104955.

Zhang, C., Li, P., Cao, B., 2017. Effects of the side groups of the spirobichroman-based diamines on the chain packing and gas separation properties of the polyimides. J. Membr. Sci. 530, 176–184.

Zhao, R., Yang, X., Li, M., Peng, X., Wei, M., Zhang, X., Yang, L., Li, J., 2021. Biodiesel preparation from Thlaspi arvense L. seed oil utilizing a novel ionic liquid core-shell magnetic catalyst. Ind. Crop. Prod. 162, 113316.